

Control of interfacial reaction and defect formation in Gd/$Bi_2Te_{2.7}Se_{0.3}$ composites with excellent thermoelectric and magnetocaloric properties

Tianchang Xue(薛天畅), Ping Wei(魏平), Chengshan Liu(刘承姗), Longzhou Li(李龙舟), Wanting Zhu(朱婉婷), Xiaolei Nie(聂晓蕾), and Wenyu Zhao(赵文俞)

Citation: Chin. Phys. B, 2024, 33 (**8**): 087403. DOI: 10.1088/1674-1056/ad4cd3

What follows is a list of articles you may be interested in

Photon number resolvability of multi-pixel superconducting nanowire single photon detectors using a single flux quantum circuit

Hou-Rong Zhou(周后荣), Kun-Jie Cheng(程昆杰), Jie Ren(任洁), Li-Xing You(尤立星),Li-Liang Ying(应利良), Xiao-Yan Yang(杨晓燕), Hao Li(李浩), and Zhen Wang(王镇)

Chin. Phys. B, 2022, 31 (**5**): 057401. DOI: 10.1088/1674-1056/ac398a

Advances in thermoelectric $(GeTe)_x(AgSbTe_2)_{100-x}$

Hongxia Liu(刘虹霞), Xinyue Zhang(张馨月), Wen Li(李文), and Yanzhong Pei(裴艳中)

Chin. Phys. B, 2022, 31 (**4**): 047401. DOI: 10.1088/1674-1056/ac3cae

Two-dimensional square-Au_2S monolayer: A promising thermoelectric material with ultralow lattice thermal conductivity and high power factor

Wei Zhang(张伟), Xiao-Qiang Zhang(张晓强), Lei Liu(刘蕾), Zhao-Qi Wang(王朝棋), and Zhi-Guo Li(李治国)

Chin. Phys. B, 2021, 30 (**7**): 077405. DOI: 10.1088/1674-1056/abe115

Electrical and thermoelectric study of two-dimensional crystal of $NbSe_2$

Xin-Qi Li(李新祺), Zhi-Lin Li(李治林), Jia-Ji Zhao(赵嘉佶), Xiao-Song Wu(吴孝松)

Chin. Phys. B, 2020, 29 (**8**): 087402. DOI: 10.1088/1674-1056/ab9614

Synthesis, physical properties, and annealing investigation of new layered Bi-chalcogenide $LaOBiHgS_3$

Yi Yu(于一), Chunchang Wang(汪春昌), Liang Li(李亮), Qiuju Li(李秋菊), Chao Cheng(程超), Shuting Wang(王舒婷), Changjin Zhang(张昌锦)

Chin. Phys. B, 2019, 28 (**1**): 017401. DOI: 10.1088/1674-1056/28/1/017401

Control of interfacial reaction and defect formation in Gd/$Bi_2Te_{2.7}Se_{0.3}$ composites with excellent thermoelectric and magnetocaloric properties

Tianchang Xue(薛天畅), Ping Wei(魏平)[†], Chengshan Liu(刘承姗), Longzhou Li(李龙舟), Wanting Zhu(朱婉婷), Xiaolei Nie(聂晓蕾), and Wenyu Zhao(赵文俞)[‡]

State Key Laboratory of Advanced Technology for Materials Synthesis and Processing, Wuhan University of Technology, Wuhan 430070, *China*

(Received 3 February 2024; revised manuscript received 9 April 2024; accepted manuscript online 17 May 2024)

The method to combine thermoelectric (TE) and magnetocaloric (MC) cooling techniques lies in developing a new material that simultaneously possesses a large TE and good MC cooling performance. In this work, using n-type $Bi_2Te_{2.7}Se_{0.3}$ (BTS) as the TE base material and Gd as the second-phase MC material, Gd/BTS composites were prepared by the spark plasma sintering method. In the composites, interfacial reaction between Gd and BTS was identified, resulting in the formation of GdTe, which has a large impact on the electron concentration through the adjustment of defect concentration. The MC/TE composite containing 2.5 wt% Gd exhibited a ZT value of 0.6 at 300 K, essentially retaining the original TE performance, while all the composites largely maintained the excellent MC performance of Gd. This work provides a potential pathway to achieving high performance in MC/TE composites.

Keywords: thermo-electro-magnetic energy conversion materials, interfacial reaction, thermoelectric performance, magnetic entropy change

PACS: 74.25.fg, 75.30.sg, 81.20.–n, 68.35.ct **DOI:** 10.1088/1674-1056/ad4cd3

1. Introduction

Since 1990, the space cooling market has been continuously growing and the number of space cooling units installed worldwide has become huge.[1,2] In recent years, solid-state cooling technologies, such as thermoelectric (TE) cooling and magnetocaloric (MC) cooling have attracted increasing attention because they avoid the use of volatile refrigerants, making cooling more environmentally friendly.

TE cooling based on the Peltier effect is achieved by creating a temperature difference between the two surfaces of a TE material when a voltage is applied. The performance of TE materials can be assessed by the dimensionless figure of merit (ZT), defined as $ZT = \alpha^2\sigma T/\kappa$, where α, σ, T and κ represent the Seebeck coefficient, electrical conductivity, absolute temperature and thermal conductivity, respectively. Hence, high-performance TE materials are characterized by high α, high σ and low κ.[3,4] Due to features such as noise-free operation, compact structure, light weight and rapid response, TE cooling is now widely commercialized in areas such as portable refrigerators, temperature sensors and integrated heat sinks.[5–7] Most commercially available TE devices are made using Bi_2Te_3-based alloys (p-type Bi–Sb–Te alloys and n-type Bi–Te–Se alloys) for TE cooling modules.[8,9] This is because Bi_2Te_3-based alloys exhibit excellent TE performance and good workability at room temperature. The equation for the coefficient of performance (COP) in cooling is $\mathrm{COP} = \frac{T_C}{T_H - T_C}\frac{\sqrt{1+\overline{ZT}} - T_H/T_C}{\sqrt{1+\overline{ZT}}+1}$, where T_C, T_H and $\overline{ZT}$ represent the cold-side temperature, the hot-side temperature and the average ZT of the TE material, respectively. According to the COP expression, to achieve a COP for TE cooling comparable to that of traditional vapor compression refrigeration in refrigerators, the ZT of TE materials needs to exceed 3.0.[10] However, the ZT of Bi_2Te_3-based alloys commonly used in the commercial sector is generally around 1.0. This low ZT and low cooling efficiency limit the application of TE cooling in large-scale cooling industries.[11]

MC cooling is another green solid-state cooling technology. It achieves cooling through magnetizing and demagnetizing cycles of MC materials. During magnetization, the material's magnetic moments become ordered with reduced magnetic entropy, thus causing the material to heat up and release heat. Conversely, during demagnetization, the magnetic moments become disordered with increased magnetic entropy, thereby cooling the material and absorbing heat.[12,13] The advantages of MC cooling technology include high efficiency, zero emissions, low noise and a large cooling capacity. As such, MC cooling technology has potential commercial applications in the refrigeration sector.[14,15] In an MC refrigerator, the core component is an active magnetic regenerator (AMR), which contains a large number of MC materials. The AMR commonly uses the metal Gd as the MC material since Gd undergoes a second-order magnetic phase transition at room temperature, which brings about a significant MC effect thereby enhancing cooling efficiency.[16,17] Most MC refrigerators use liquid as the cooling medium, but many more environmentally

[†]Corresponding author. E-mail: pingwei@whut.edu.cn
[‡]Corresponding author. E-mail: wyzhao@whut.edu.cn

© 2024 Chinese Physical Society and IOP Publishing Ltd

friendly solid cooling media have been developed, such as plate-shaped compound magnetic refrigerants.[18] These media effectively assist in heat exchange during the magnetization and demagnetization processes of MC materials. However, thermal exchange between MC materials and the cooling medium, including conduction and convection, leads to cycle heat losses. These heat losses limit the cycle frequency of MC cooling and result in a lower cooling power density.[19] Despite the many advantages of MC cooling technology, the aforementioned efficiency limitations make it challenging for MC cooling to compete with traditional vapor compression refrigeration. Therefore, how to enhance the heat exchange efficiency and cycle frequency of MC cooling technology is of great importance for achieving a higher COP for MC applications.

Both TE and MC technologies excel in specific application domains, but due to limitations in efficiency, cost and applicability they struggle to independently replace existing vapor compression refrigeration techniques. To overcome these limitations, a new cooling technology pathway has emerged, namely, MC/TE hybrid cooling technology.[20] This approach combines the benefits of TE and MC cooling with the aim of enhancing overall cooling efficiency and performance through the synergistic operation of both technologies.[21,22]

However, this combination also introduces its own set of challenges. At the device level, integrating TE and MC technologies might lead to issues such as thermal leakage and Joule heating generated by TE modules. These issues could reduce the overall system efficiency and increase energy consumption. Additionally, designing an efficient MC/TE hybrid system poses significant challenges. It demands the development of materials that exhibit high TE and MC performance simultaneously. These materials need to operate efficiently in their respective cooling cycles while maintaining good thermal stability and mechanical properties.[23] In practical applications, such material design and optimization require a comprehensive consideration of the physical, chemical and thermodynamic properties, a task that is quite challenging in the field of material science and engineering.[24,25] Wei *et al*. conducted a material preparation and interfacial microstructure study of Gd/$Bi_{0.37}Sb_{1.63}Te_3$, an MC/TE composite material.[26] Wang *et al*. investigated the stability of Gd/$Bi_{0.5}Sb_{1.5}Te_3$ in a service environment.[27] Recently, the TE and MC properties of $La(Fe_{0.92}Co_{0.08})_{11.9}Si_{1.1}$/BiSbTe and MnCoGe/BiSbTe composite materials were reported.[28,29] These studies not only analyzed the effects of different contents and sintering temperatures on the performance and phase composition of these materials but also paid special attention to the impact of interface reactions and elemental diffusion on MC performance. The results indicated that these micrometer-scale interactions have a significant impact on the MC performance of the composite materials. Note that all the relevant research has primarily focused on the composite of p-type Bi_2Te_3-based alloys with MC materials.[23–26] These findings have provided a valuable knowledge base for the development of MC/TE hybrid cooling technology. However, it is noteworthy that, to date, research on the composite of n-type Bi_2Te_3-based alloys with MC materials is relatively scarce. Therefore, investigating the impact of incorporating MC materials on the TE performance of n-type Bi_2Te_3-based alloys is of significant interest. Additionally, how MC materials retain their MC properties in MC/TE composite materials, and how heterogeneous interfaces affect electron and thermal transport, are topics of considerable research value.

This work focused on using n-type $Bi_2Te_{2.7}Se_{0.3}$ (BTS) as the TE matrix and Gd spheres as the MC second phase to synthesize a series of MC/TE composites. The thermal, electrical and magnetic properties of these MC/TE composites were investigated. The formation of an interfacial reaction layer between the TE matrix and Gd spheres caused the creation of defects while modulating the electron concentration. The MC/TE composites containing 2.5 wt% Gd exhibited a ZT value of 0.6 at 300 K, essentially retaining the performance of the original TE material. Additionally, all composites largely maintained the excellent MC performance of Gd.

2. Experiment

2.1. Sample preparation

A series of MC/TE composites xGd/BTS with different mass fractions of Gd ($x = 0\%$, 2.5%, 5.0%, 7.5%, 10.0%) were prepared using the spark plasma sintering method. Bi (4N, 60 mesh powder), Te (4N, 60 mesh powder), Se (4N, 60 mesh powder) and Ag (5N, powder) in the stoichiometric ratio $Ag_{0.006}Bi_2Te_{2.7}Se_{0.3}$ were weighted. The weighted elements were sealed in a quartz glass tube under vacuum and placed in a muffle furnace at 1073 K to melt for 24 h. After quenching, a polycrystalline ingot of $Ag_{0.006}Bi_2Te_{2.7}Se_{0.3}$ was obtained. The ingot was crushed and ground, followed by sieving through a 120-mesh screen to prepare BTS alloy powder with an approximate particle size of 120 μm. To avoid particle segregation leading to uneven mixing of the two phases,[30] Gd spheres with a particle size of 120 ± 30 μm were selected. The BTS powder was mixed with Gd spheres at different mass ratios, then ultrasonically dispersed in alcohol and dried to obtain uniformly mixed powders. To fully utilize the MC properties of the composites, a larger amount of composite was chosen. To suppress the heterogeneous interfacial reaction between Gd and BTS, a low-temperature high-pressure sintering method was selected as follows: the Gd/BTS composite powder was loaded into a cylindrical die made of tungsten carbide and sintered at 600 K under a high axial pressure of 200 MPa.

2.2. Characterization and measurements

The phase composition of Gd/BTS composites was analyzed using Cu $K_{\alpha 1}$ radiation ($\lambda = 1.54186$ Å) through x-ray diffraction (XRD; SmartLab, Rigaku Corporation, Tokyo, Japan). The microstructure and elemental mapping of the reaction interface between Gd and BTS were characterized using an electron probe microanalyzer (EPMA; JXA-8230, JEOL). The thermomagnetic curves (M–T curves) and Arrott plots of the composites were measured using the vibrating sample magnetometer (VSM) module of Versalab, manufactured by Quantum Design, USA. The magnetic entropy change $\Delta S_{\rm m}$ was calculated based on the magnetization curves obtained from the VSM. The electrical conductivity (σ) and Seebeck coefficient (α) were simultaneously measured from 300 K to 500 K under a helium atmosphere using the standard four-probe method (Cryoall CTA-3/500). The thermal conductivity (κ) of the samples was calculated using the formula $\kappa = \lambda \rho C_{\rm p}$, where ρ is the volume density measured by the Archimedes method, $C_{\rm p}$ is the specific heat capacity calculated using the Dulong–Petit law and λ is the thermal diffusivity measured using the laser flash technique (Netzsch LFA-467). The carrier thermal conductivity ($\kappa_{\rm C}$) of the samples was calculated using the Wiedemann–Franz law $\kappa_{\rm C} = L\sigma T$, where L is the Lorenz number calculated according to the equation $L = 1.5 + \exp(-|\alpha|/116)$. The lattice thermal conductivity ($\kappa_{\rm L}$) of the samples was determined by $\kappa_{\rm L} = \kappa - \kappa_{\rm C}$. The Hall effect coefficient ($R_{\rm H}$) was measured on a Hall testing system (NYMS-1) and the carrier concentration (n) and mobility (μ) were calculated using the equations $n = |1/(R_{\rm H}e)|$ and $\mu = |\sigma R_{\rm H}|$, respectively, where e is the electronic charge.

3. Results and discussion

3.1. Phase constituents and microstructures

Figure 1 shows the XRD patterns of the Gd/BTS composites. Comparing the characteristic diffraction peaks of the composites with the standard data of $Bi_2Te_{2.7}Se_{0.3}$ (JCPDS No. 50-0954), it is observed that the characteristic diffraction peaks for all composites correspond to the standard without an obvious peak shift. This result indicates that the introduction of metallic Gd to the BTS matrix does not alter the crystal structure of BTS. A characteristic diffraction peak of Gd appears near 32.5° for the 10% Gd/BTS sample, while this is not observed in the other samples. This result is understandable because of the much lower amount of Gd in the composite.

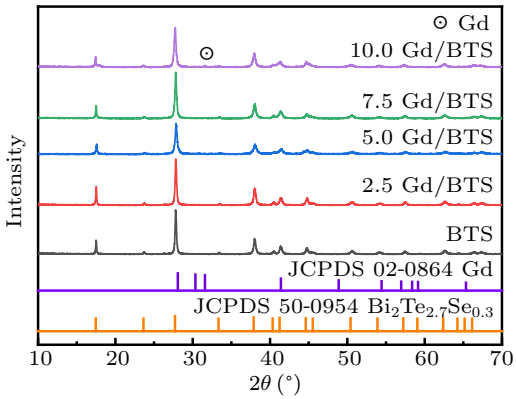


Fig. 1. XRD patterns of Gd/BTS composites prepared by the spark plasma sintering method.

To investigate the interfacial reaction between Gd and BTS, the microstructure and elemental mapping near the Gd–BTS interface were characterized by electron probe microanalysis (EPMA). The secondary electron image (SEI) (Fig. 2(a)) and backscattered electron image (BEI) (Fig. 2(b)) clearly reveal the formation of a thin interfacial reaction layer at the interface between the matrix and Gd spheres. It can be seen that the thickness of the interfacial reaction layer near the Gd sphere is uneven. The elemental mappings of Bi, Te, Se and Gd are shown in Figs. 2(c)–2(f). This analysis confirmed that the interfacial reaction layer consisted of Gd and Te without the presence of Bi and Se.

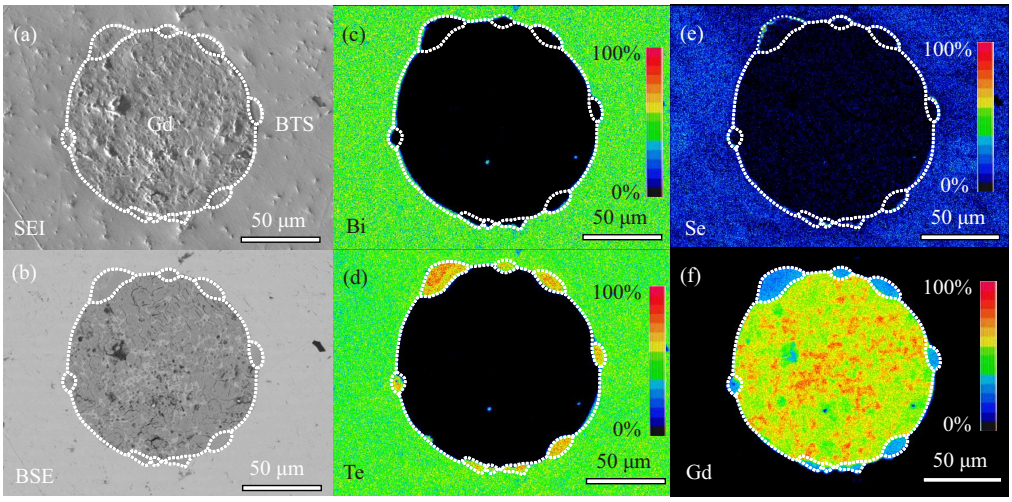


Fig. 2. Interfacial microstructure between Gd and BTS in 2.5% Gd/BTS: (a) secondary electron image; (b) backscattered electron image. (c)–(f) Elemental mappings of Bi, Te, Se and Gd.

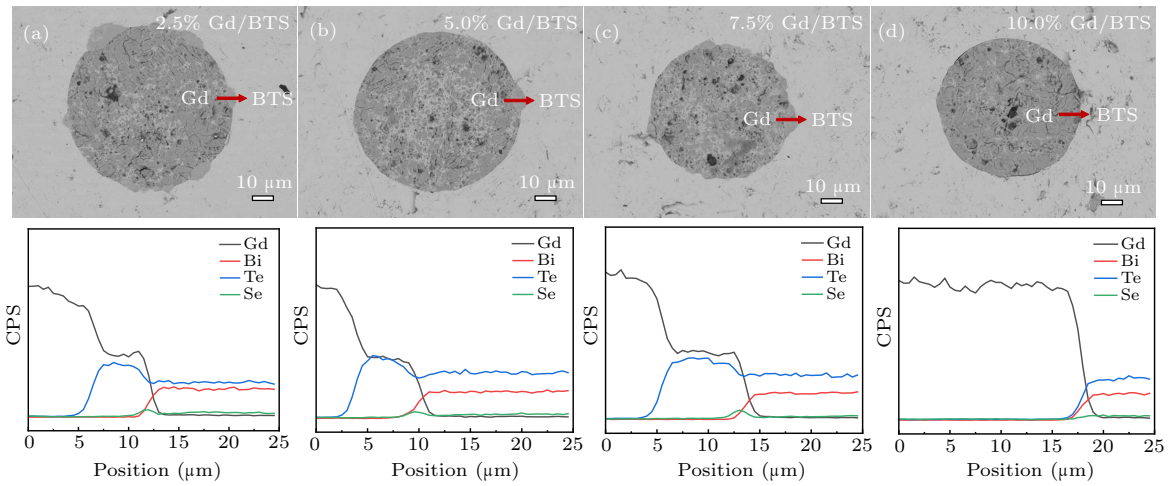


Fig. 3. Backscattered electron images and corresponding elemental line scans at the interfaces of *x*Gd/BTS composites: (a) 2.5% Gd/BTS, (b) 5.0% Gd/BTS, (c) 7.5% Gd/BTS, (d) 10.0% Gd/BTS.

BEIs and energy dispersive x-ray spectroscopy (EDS) line scans around the Gd spheres were measured to analyze the interfacial reaction layer. The results, shown in Fig. 3, indicate that the interfacial reaction layer is composed of Gd and Te with a Gd:Te ratio very close to 1:1, confirming the formation of GdTe at the heterogeneous interfaces. The EDS line scan shown in Fig. 3(d) did not detect the existence of an interfacial reaction layer, suggesting that some Gd/BTS interfaces remained unreacted. It was observed that the thickness of the interfacial reaction layer near the Gd sphere was uneven, with a large average thickness of about 9.0–10.0 μm, indicating no significant difference in the thickness of the interface reaction layer among different samples. Therefore, as the mass fraction of Gd increases in the composites, the content of the GdTe phase also increases. It is interesting that the structure of the heterogeneous interface between Gd and BTS matrix is very similar to that between Gd and a p-type bismuth telluride matrix.[23]

3.2. Magnetocaloric properties

Figure 4 shows the magnetic properties of metallic Gd and Gd/BTS composites measured under extended magnetic fields. The thermomagnetic (M–T) curves imply that the Curie temperature (T_C) of the Gd/BTS composites is approximately 293 K, equal to that of Gd (Figs. 4(a) and 4(b)). The magnetic field dependence of the magnetization curves was measured under external magnetic fields ranging from 0 to 2.5 T within a temperature range of 251–329 K. Using Arrott plots (M^2–H/M curves) the magnetic phase transitions can be determined. The Arrott plots of Gd and the Gd/BTS composites are displayed in Figs. 4(c) and 4(d). According to Banerjee's criterion, a negative slope or S-shaped profile of the M^2–H/M curves near T_C suggests a first-order magnetic phase transition, while a positive slope of these curves implies a second-order magnetic phase transition.[31] The Arrott plots of Gd and Gd/BTS composites both exhibit positive slopes, implying their second-order magnetic phase transition characteristics. It can therefore be seen that although interfacial reaction takes place the compositing of Gd with BTS has less impact on the magnetic phase transition of the composites.

According to the Maxwell relation,

$$\Delta S(T,H) = S(T,H) - S(T,0) = \int_0^H \frac{\mathrm{d}M}{\mathrm{d}T}\,\mathrm{d}H,$$

ΔS is defined as a function of temperature and magnetic field. It can be seen that ΔS is closely related to the magnetic properties of the MC material. Figure 5(a) shows ΔS of Gd under external magnetic fields ranging from 0 to 2.5 T. Figure 5(b) compares ΔS for Gd/BTS composites and the corresponding mass fraction of Gd under an external magnetic field of 2.5 T, while Table 1 summarizes the corresponding MC properties. For Gd and Gd/BTS composites, ΔS gradually rises as the temperature increases, reaching a maximum (ΔS_m) at the Curie point (T_C), and then decreases, with a higher mass fraction causing an increase in ΔS_m. For Gd/BTS composites, the results indicate that the T_C of all composites is around 293 K, consistent with the T_C of Gd. With an increase in the amount of Gd, the difference between the ΔS_m of Gd/BTS composites and the ΔS_m of the corresponding mass fraction of Gd increases. Figure 5(c) shows the loss rate of ΔS_m of Gd/BTS composites under different mass fractions of Gd. With the increase in mass fraction of Gd, the loss rate of ΔS_m also increases monotonously. This indicates that the increase in heterogeneous interfaces will lead to greater ΔS_m loss of Gd/BTS composites. The ΔS_m of 2.5% Gd/BTS composite is 0.15 $\mathrm{J{\cdot}kg^{-1}{\cdot}K^{-1}}$, while that of theoretical 2.5 wt% Gd is 0.16 $\mathrm{J{\cdot}kg^{-1}{\cdot}K^{-1}}$, indicating a loss rate of ΔS_m about 6% for the Gd/BTS composite, essentially maintaining the MC performance of Gd. The ΔS_m of 10.0% Gd/BTS composite is 0.54 $\mathrm{J{\cdot}kg^{-1}{\cdot}K^{-1}}$, and that of theoretical 10.0 wt% Gd is 0.60 $\mathrm{J{\cdot}kg^{-1}{\cdot}K^{-1}}$, resulting in a loss rate of ΔS_m of about 9.4%. Relative cooling power (RCP) represents the heat transferred

from the heat reservoir to the cold reservoir and is commonly used to assess the MC properties of materials.[32] The RCP is defined as follows: RCP $= \int_{T_2}^{T_1} |\Delta S_m| dT$, where the temperature ranges from T_1 to T_2. Although an increase in the composite amount of Gd may result in greater loss of MC properties, the loss rate of MC properties of 10% Gd/BTS is 9.6%, which is still a relatively low level. Therefore, the MC performance of the Gd/BTS composites studied in this work could be well maintained, which is necessary for developing high-performance thermo-electromagnetic materials.

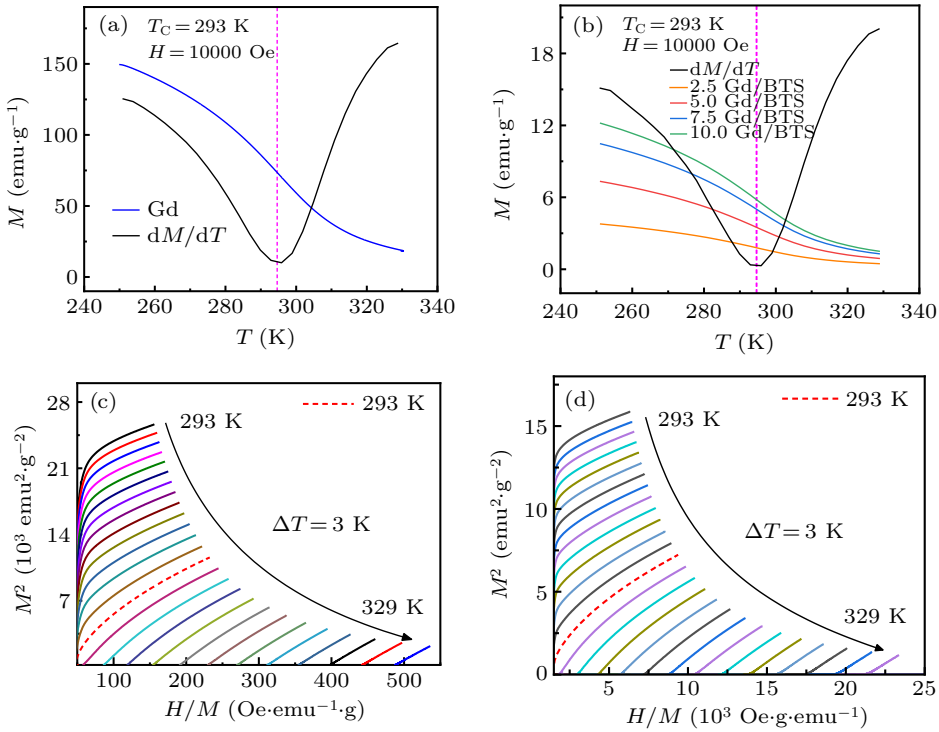


Fig. 4. Magnetic properties of Gd and Gd/BTS composites. (a) M–T thermomagnetic curves and corresponding differential curves measured at 10000 Oe. (b) M–T thermomagnetic curves and corresponding differential curves of Gd/BTS composites measured at 10000 Oe. (c) Arrott plots of Gd, measured over the range 251–329 K at 3 K intervals. (d) Arrott plots of xGd/BTS composites, measured over the range 251–329 K at 3 K intervals.

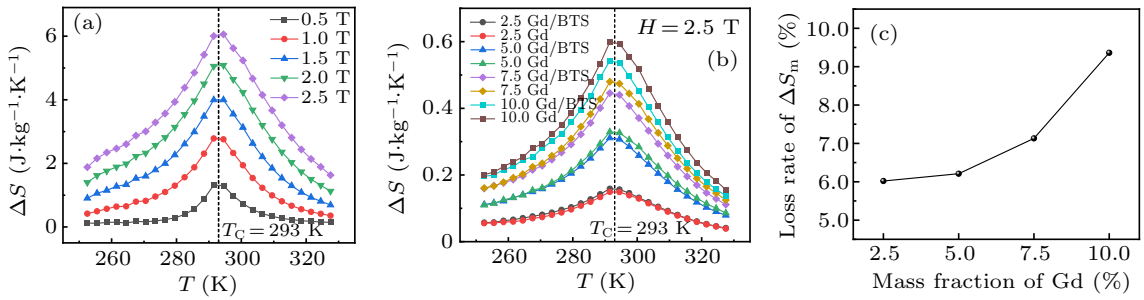


Fig. 5. Magnetic entropy of Gd and Gd/BTS composites. (a) Magnetic entropy change ΔS of Gd under an external magnetic field ranging from 0 to 2.5 T. (b) Magnetic entropy change ΔS of Gd/BTS composites and corresponding mass fractions of Gd under an external magnetic field of 2.5 T. The ΔS data for xGd are obtained by multiplying the ΔS data for Gd by x%. (c) Loss rate of maximal magnetic entropy ΔS_m of Gd/BTS composite material with different mass fractions of Gd.

Table 1. Magnetocaloric properties of xGd/BST composites and xGd.

Sample	ΔS_m (J·kg^{-1}·K^{-1})	RCP (J·kg^{-1})
2.5 Gd/BTS	0.149	6.34
2.5 Gd	0.159[a)]	6.77[a)]
5.0 Gd/BTS	0.311	13.21
5.0 Gd	0.329[a)]	13.97[a)]
7.5 Gd/BTS	0.446	18.88
7.5 Gd	0.480[a)]	20.32[a)]
10.0 Gd/BTS	0.542	22.94
10.0 Gd	0.599[a)]	25.40[a)]

The ΔS_m of xGd/BST are obtained under an applied magnetic field of 2.5 T.
[a)]The ΔS_m data of xGd are obtained by multiplying the ΔS_m data for Gd by x%.

3.3. Thermoelectric properties

Figure 6 displays the temperature dependence of the Hall coefficient (R_H), carrier concentration (n), mobility (μ), electrical conductivity (σ), Seebeck coefficient (α) and power factor ($\alpha^2\sigma$) of Gd/BTS composites in the temperature range 300–500 K. The temperature dependence of R_H (Fig. 6(a)) indicates that the majority of carriers are electrons, implying an n-type conductive behavior. As shown in Fig. 6(b), and attributed to the enhanced intrinsic excitation at elevated temperatures, the n of all composites increases with the rise in test

temperature, resulting in the generation of more electron–hole pairs across the band gap.[33] n becomes similar when the test temperature increases to 500 K. The reasons for the similarity are as follows: (1) The n of BTS is high, which suppresses its intrinsic excitation. Thus, intrinsic excitations are not significant throughout the entire temperature range and the carrier concentration of BTS remains relatively constant. (2) As x increases, n decreases, and the temperature of intrinsic excitation also decreases. Consequently, intrinsic excitations become more pronounced with increasing x, leading to the convergence of n in different composites at high temperatures.

Compositing Gd with BTS results in a significant decrease in n. With the increase in x, n monotonically decreases. The decrease in carriers should be closely related to the interface reaction. According to the research conducted by Liu *et al.*, the formation of an interfacial reaction layer produces antisite defects.[34] The generation of defects consumes electrons and generates holes, leading to a decrease in n. The defect reactions are represented by

$$\mathrm{Gd} + \mathrm{Te}_{\mathrm{Te}}^{\times} \rightarrow \mathrm{GdTe} + \mathrm{V}_{\mathrm{Te}}^{\cdot\cdot} + 2\mathrm{e}', \quad (1)$$

$$\mathrm{Bi}_{\mathrm{Bi}}^{\times} + \mathrm{V}_{\mathrm{Te}}^{\cdot\cdot} + 2\mathrm{e}' \rightarrow \mathrm{Bi}_{\mathrm{Te}}' + \mathrm{V}_{\mathrm{Bi}}''' + 4\mathrm{h}^{\cdot}, \quad (2)$$

where $\mathrm{Bi}_{\mathrm{Bi}}^{\times}$, $\mathrm{V}_{\mathrm{Te}}^{\cdot\cdot}$, e', $\mathrm{Bi}_{\mathrm{Te}}'$, $\mathrm{V}_{\mathrm{Bi}}'''$ and $\mathrm{h}^{\cdot}$ respectively represent a normal Bi atom, Te vacancy, electron, antisite defect (Bi on Te site), Bi vacancy and hole. Moreover, based on the theory of metal–semiconductor contacts,[35] as the work function of GdTe (5.7 eV)[36] is greater than that of n-type Bi_2Te_3 (5.13 eV) and Gd (2.9 eV),[37] electrons tend to transfer from n-type Bi_2Te_3 and Gd to GdTe, leading to a decrease in carrier concentration. Therefore, with increasing x, the content of the GdTe phase increases, and a greater influx of electrons into the GdTe phase and increase in the concentration of antisite defects are expected, consequently resulting in a decrease of n.

As shown in Fig. 6(c), the μ of all composites decreases with the increase in test temperature, as elevated temperatures enhance lattice vibrations.[38] The variation in μ is a coupled result of carrier and interface scattering. The μ at room temperature for 2.5% Gd/BTS is increased compared with BTS. The introduction of Gd significantly reduces n, optimizes carrier scattering and leads to an increase in μ.[39] For $x \geq 5\%$, μ at room temperature decreases relative to BTS. When x is high, there are too many heterogeneous interfaces, which results in enhanced interface scattering and decreased μ.[40]

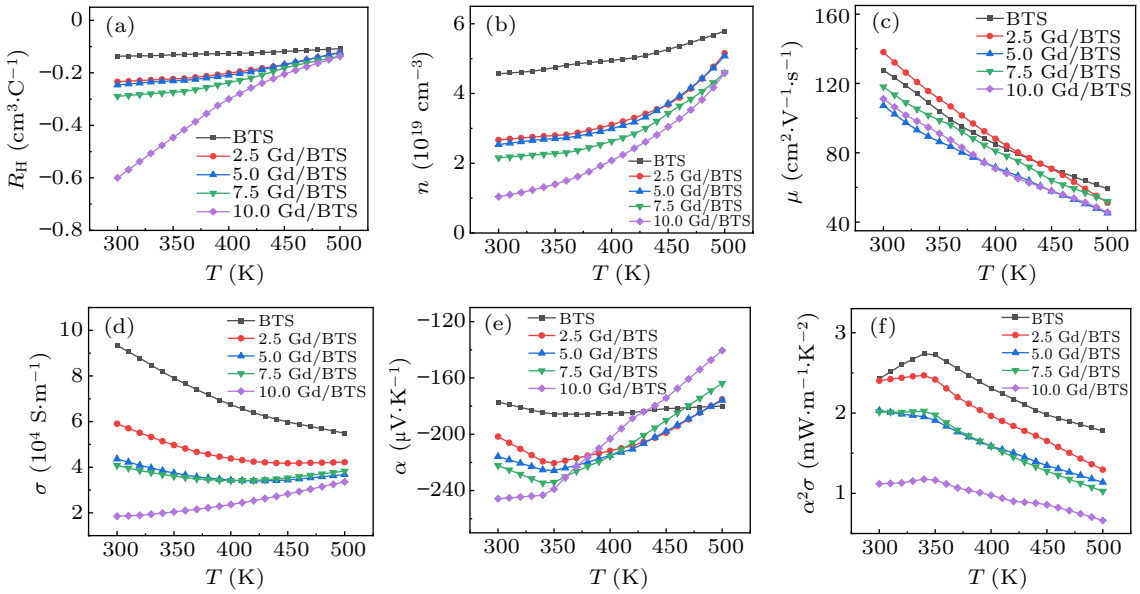


Fig. 6. Electrical transport properties of Gd/BTS composites. Temperature dependence of (a) Hall coefficient (R_H), (b) carrier concentration (n), (c) mobility (μ), (d) electrical conductivity (σ), (e) Seebeck coefficient (α) and (f) power factor ($\alpha^2\sigma$).

As depicted in Fig. 6(d), the room-temperature σ of the Gd/BTS composites monotonically decreases with increasing x, which should be attributed to the increase in heterogeneous interfaces and the resultant reduction in n.[33] As shown in Fig. 6(e), all composites exhibit a negative α, indicating n-type conductive behavior of Gd/BTS, in consistent with the Hall measurement. At room temperature, the absolute value of α monotonically increases with x due to the reduction in n. According to the temperature dependence of lattice thermal conductivity (Fig. 7(c)), the intrinsic excitation temperatures of BTS, 2.5% Gd/BTS, 5.0% Gd/BTS and 7.5% Gd/BTS are around 350 K. Consequently, the absolute value of α initially increases with rising test temperature and then decreases at around 350 K due to intrinsic excitation. The 10.0% Gd/BTS exhibits intrinsic excitation behavior from room temperature, resulting in a monotonic decrease in the absolute value of α with increasing test temperature. As shown in Fig. 6(f), the room-temperature $\alpha^2\sigma$ of the Gd/BTS composites decreases monotonically with increasing x. A large decrease in σ should be responsible. The $\alpha^2\sigma$ of BTS at 300 K is approximately

2.42 mW·K^{-2}·m^{-1}, while for 2.5% Gd/BTS at 300 K it is about 2.40 mW·K^{-2}·m^{-1}, a slight decrease. It can be inferred that a further improvement in n is necessary, as it plays a crucial role in determining the electron transport properties of Gd/BTS composites.

The thermal transport properties and ZT values of Gd/BTS composites in the temperature range 300–500 K are shown in Fig. 7. With an increase in x, the total thermal conductivity (κ) near room temperature increases at first and then decreases. The carrier thermal conductivity (κ_C) significantly decreases with increasing x, and this trend is consistent with the behavior of σ. The lattice thermal conductivity (κ_L) of Gd/BTS composites increases with x, predominantly influenced by the high thermal conductivity value of Gd itself when Gd composite is abundant. The κ_L of Gd/BTS composites decreases with increasing test temperature, closely related to the enhancement of phonon–phonon interactions at elevated temperatures. With further increase in temperature, κ_L rapidly increases, indicating the dominance of bipolar thermal diffusion at this stage.[41] For the 10% Gd/BTS composite, κ_L monotonically increases with temperature, suggesting that the material enters the intrinsic excitation region even at room temperature. The low intrinsic excitation temperature should be accounted for by low carrier concentration. The ZT value of 2.5% Gd/BTS is nearly equal to that of BTS matrix, at around 0.6. This indicates that when BTS is used as the matrix and combined with a low mass fraction of Gd spheres, a high ZT can be obtained for the MC/TE composites.

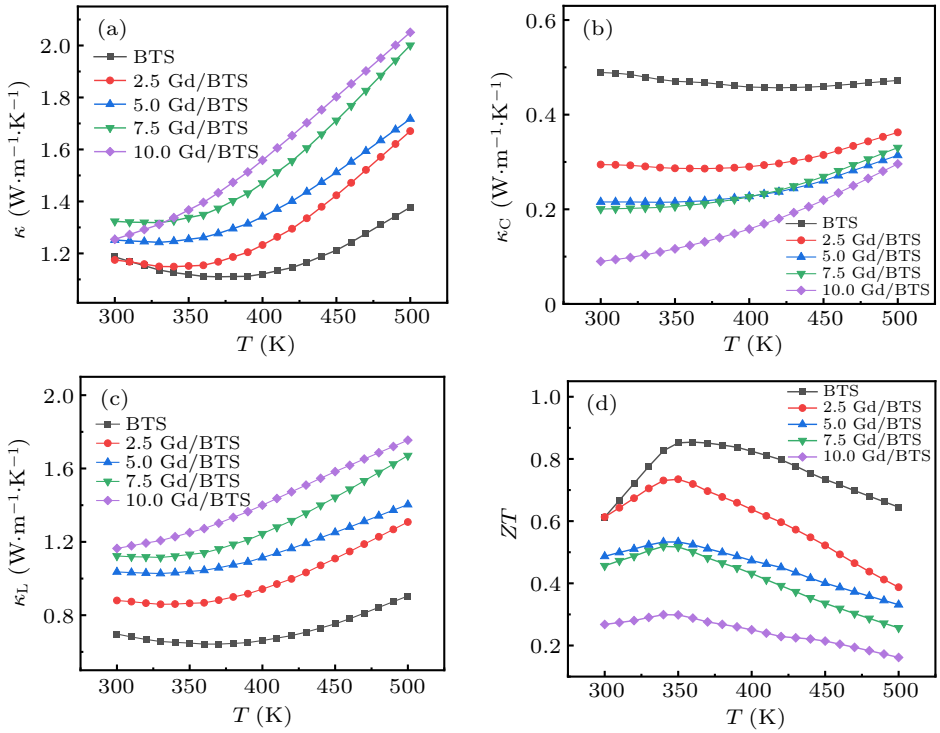


Fig. 7. Temperature dependence of thermal transport properties and ZT of Gd/BTS composites: (a) total thermal conductivity (κ), (b) carrier thermal conductivity (κ_C), (c) lattice thermal conductivity (κ_L) and (d) ZT.

4. Conclusions

In summary, in this work we employed a low-temperature high-pressure spark plasma sintering process to prepare a series of Gd/BTS composites. XRD results indicated that Gd, as a secondary phase, did not affect the crystal structure of BTS. In Gd/BTS composites, an interfacial reaction layer composed of Gd and Te, with a Gd:Te ratio of 1:1, was found to be distributed around the surface of the Gd spheres. Both MC and TE performances were significantly affected by the interfacial reaction layers during the fabrication of the composites. The results showed that 2.5% Gd/BTS MC/TE composites and BTS both exhibited a ZT of 0.6 at 300 K, essentially retaining the TE performance prior to compositing. All the composites largely maintained the excellent MC performance of Gd but a high Gd content poisoned the TE performance. This work provides a promising pathway for achieving high TE performance in n-type MC/TE composites.

Acknowledgements

Project supported by the National Key Research and Development Program of China (Grant Nos. 2019YFA0704900 and 2023YFB3809400), the National Natural Science Foundation of China (Grant Nos. 52130203 and 52172232), and the Basic and Applied Basic Research Foundation of Guangdong Province (Grant No. 2022B1515120005).

References

[1] Pezzutto S, De Felice M, Fazeli R, Kranzl L and Zambotti S 2017 *Energies* **10** 1253

[2] Pezzutto S, Fazeli R, De Felice M and Sparber W 2016 *WIREs Energy Environ.* **5** 649

[3] Yang L, Chen Z G, Dargusch M S and Zou J 2017 *Adv. Energy Mater.* **8** 1701797

[4] He J and Tritt T M 2017 *Science* **357** 1369 eaak9997

[5] Wang C Y, Zhang Y X, Han F and Jiang Z D 2023 *Micromachines* **14** 1853

[6] Alam N, Salman Ali M, Sajid S, Sharma D and Hasan Z 2023 *Sol. Energy* **263** 111892

[7] Chen W Y, Shi X, Zou J and Chen Z G 2022 *Small Methods* **6** 2101235

[8] Witting I T, Chasapis T C, Ricci F, Peters M, Heinz N A, Hautier G and Snyder G J 2019 *Adv. Electronic Mater.* **5** 1800904

[9] Hong M, Chen Z G and Zou J 2018 *Chin. Phys. B* **27** 48403

[10] Mao J, Chen G and Ren Z F 2021 *Nat. Mater.* **20** 454

[11] Saberi Y and Sajjadi S A 2022 *J. Alloys Compd.* **904** 163918

[12] Greco A, Farina A R and Masselli C 2021 *Italian J. Eng. Sci.* **65** 58

[13] Ram N R, Prakash M, Naresh U, Kumar N S, Sarmash T S, Subbarao T, Kumar R J, Kumar G R and Naidu K C B 2018 *J. Supercond. Nov. Magn.* **31** 1971

[14] Kitanovski A, Plaznik U, Tomc U and Poredoš A 2015 *Int. J. Refrig.* **57** 288

[15] Gschneidner K A and Pecharsky V K 2008 *Int. J. Refrig.* **31** 945

[16] Dall'olio S, Masche M, Liang J, Insinga A R, Eriksen D K, Bjørk R, Nielsen K K, Barcza A, Vieyra H A, Beek N V, Bez H N, Engelbrecht K and Bahl C R H 2021 *Int. J. Refrig.* **132** 243

[17] Kitanovski A 2020 *Adv. Energy Mater.* **10** 1903741

[18] Xu S S, Fu Q, Zhou Y F, Peng L, Gao X Q, Li Z X, Gong M Q, Dong X Q and Shen J 2023 *Chin. Phys. B* **32** 27502

[19] Kamran M S, Ahmad H O and Wang H S 2020 *Renew. Sust. Energ. Rev.* **133** 110247

[20] Wei P, Li L Z, Zhu W T, Nie X L, Zhang J Q, Zhao W Y and Zhang Q J 2022 *Mater. China* **41** 965

[21] Tomc U, Tušek J, Kitanovski A and Poredoš A 2013 *Appl. Therm. Eng.* **58** 1

[22] Monfared B 2017 *Int. J. Refrig.* **74** 324

[23] Li C C, Zhao W Y and Zhang Q J 2022 *Sci. Bull.* **67** 891

[24] Tan G, Zhao L D and Kanatzidis M G 2016 *Chem. Rev.* **116** 12123

[25] Scheibel F, Gottschall T, Taubel A, Fries M, Skokov K P, Terwey A, Keune W, Ollefs K, Wende H, Farle M, Acet M, Gutfleisch O and Gruner M E 2018 *Energy Technol.* **6** 1397

[26] Wei P, Ke B, Xing L, Li C C, Ma S F, Nie X L, Zhu W T, Sang X H, Zhang Q J, Van Tendeloo G and Zhao W Y 2020 *Mater. Charact.* **163** 110240

[27] Wang B, Yu J, Li C C, Nie X L, Zhu W T, Wei P, Zhao W Y and Zhang Q J 2023 *J. Inorg. Mater.* **38** 663

[28] Xing L, Cui W J, Sang X H, Hu F X, Wei P, Zhu W T, Nie X L, Zhang Q J and Zhao W Y 2021 *J. Materiomics* **7** 998

[29] Li L Z, Wei P, Ke B, Nie X L, Zhu W, Zhao W Y and Zhang Q J 2023 *Mater. Charact.* **199** 112760

[30] Li M, An X Z and Wu Y H 2023 *Adv. Powder Technol.* **34** 103953

[31] Burrola-Gándara L A, Santillan-Rodriguez C R, Rivera-Gomez F J, Saenz-Hernandez R J, Botello-Zubiate M E and Matutes-Aquino J A 2015 *J. Appl. Phys.* **117** 17D144

[32] Franco V, Blázquez J S, Ingale B and Conde A 2012 *Annu. Rev. Mater. Res.* **42** 305

[33] Gayner C and Kar K K 2016 *Prog. Mater Sci.* **83** 330

[34] Liu C S, Xu W J, Wei P, Ke S Q, Cui W J, Li L Z, Liang D, Ye X F, Chen T T, Nie X L, Zhu W, Zhao W Y and Zhang Q J 2024 *Energy Environ. Mater.* **0** 12710

[35] Rhoderick E H and Rothwarf A 1979 *Phys. Today* **32** 66

[36] Ahamed I, Chauhan Y S, Bhowmick S and Agarwal A 2023 *Com. Mater. Sci.* **216** 111869

[37] Ryu B 2018 *J. Korean Phy. Soc.* **72** 122

[38] Zhu Y K, Jin Y F, Zhu J B, Dong X Y, Liu M, Sun Y X, Guo M C, Li F S, Guo F K, Zhang Q, Liu Z H, Cai W and Sui J H 2023 *Adv. Sci.* **10** 2206395

[39] Hu C L, Xia K Y, Fu C G, Zhao X B and Zhu T J 2022 *Energy Environ. Sci.* **15** 1406

[40] Li S K, Liu Y D, Liu F S, He D S, He J Q, Luo J, Xiao Y G and Pan F 2018 *Nano Energy* **49** 257

[41] Samanta M, Pal K, Waghmare U V and Biswas K 2020 *Angew. Chem. Int. Ed.* **59** 4822